

Article

Band Bending and Trap Distribution along the Channel of Organic Field-Effect Transistors from Frequency-Resolved Scanning Photocurrent Microscopy

Gion Kalemai, Nikolaos Vagenas, Athina Giannopoulou and Panagiotis Kounavis * 

Department of Electrical and Computer Engineering, University of Patras, 26504 Patras, Greece; ece8059@upnet.gr (G.K.); vagenasn@ece.upatras.gr (N.V.); athgian@upatras.gr (A.G.)

* Correspondence: pkounavis@upatras.gr

Abstract: The scanning photocurrent microscopy (SPCM) method is applied to pentacene field-effect transistors (FETs). In this technique, a modulated laser beam is focused and scanned along the channel of the transistors. The resulting spatial photocurrent profile is attributed to extra free holes generated from the dissociation of light-created excitons after their interaction with trapped holes. The trapped holes result from the local upward band bending in the accumulation layer depending on the applied voltages. Thus, the photocurrent profile along the conducting channel of the transistors reflects the pattern of the trapped holes and upward band bending under the various operating conditions of the transistor. Moreover, it is found here that the frequency-resolved SPCM (FR-SPCM) is related to the interaction of free holes via trapping and thermal release from active probed traps of the first pentacene monolayers in the accumulation layer. The active probed traps are selected by the modulation frequency of the laser beam so that the FR-SPCM can be applied as a spectroscopic technique to determine the energy distribution of the traps along the transistor channel. In addition, a crossover is found in the FR-SPCM spectra that signifies the transition from empty to partially empty probed trapping states near the corresponding trap quasi-Fermi level. From the frequency of this crossover, the energy gap from the quasi-Fermi E_{tp} level to the corresponding local valence band edge E_v , which is bent up by the gate voltage, can be estimated. This allows us to spatially determine the magnitude of the band bending under different operation conditions along the channel of the organic transistors.

Keywords: organic field-effect transistors; band bending; trap distribution



Citation: Kalemai, G.; Vagenas, N.; Giannopoulou, A.; Kounavis, P. Band Bending and Trap Distribution along the Channel of Organic Field-Effect Transistors from Frequency-Resolved Scanning Photocurrent Microscopy. *Electronics* **2022**, *11*, 1799. <https://doi.org/10.3390/electronics11111799>

Academic Editor: Antonio Di Bartolomeo

Received: 30 April 2022

Accepted: 2 June 2022

Published: 6 June 2022

Publisher's Note: MDPI stays neutral with regard to jurisdictional claims in published maps and institutional affiliations.



Copyright: © 2022 by the authors. Licensee MDPI, Basel, Switzerland. This article is an open access article distributed under the terms and conditions of the Creative Commons Attribution (CC BY) license (<https://creativecommons.org/licenses/by/4.0/>).

1. Introduction

Over the past three decades, significant progress has been made in organic semiconductors, and organic devices have been fabricated with improved performance making them competitive or complementary to conventional silicon-based devices [1]. The organic field-effect transistor (OFET) is the basic building block of organic electronics [2]. Intensive research focused on improving organic materials as well as the device fabrication process has resulted in OFETs with improved performance and high mobilities that are comparable to or even better than those of amorphous silicon-based devices [3]. The intrinsic properties of organic materials are not the only factors that are important for improving the performance of OFETs. There are other critical parameters, such as the contact interface and the semiconductor–insulator interface, which can seriously limit the performance of OFETs [4,5]. Energy barriers at the contacts can prevent carrier injection and modify the lateral electric-field distribution along the conducting channel of the transistors by the drain–source voltage V_{DS} [6]. The presence of trapped carriers at the insulator interface can affect the turn-on voltage, the vertical electric field from the applied gate-source voltage V_{GS} , and the band bending in the charge accumulation layer [7].

Scanning photocurrent microscopy (SPCM) is a technique suitable for spatially monitoring the complex interrelating phenomena at the contacts and insulator interfaces of OFETs. In this technique, a laser beam is focused onto the transistor channel either in the form of a line-shaped laser beam or in the form of a diffraction-limited point-like laser beam, which is scanned along the channel [8]. The intensity of the laser beam is modulated by producing a modulated source–drain current or modulated photocurrent, also called the SPCM signal. In pentacene FETs, inhomogeneous SPCM signal profiles were found along the source contact, attributed to enhanced exciton dissociation and a reduced injection barrier [9]. In other pentacene FETs, a strong SPCM signal was observed near both contact edges, which was explained by a high contact resistance due to energy barriers [10,11]. In some pentacene FETs, a structured SPCM signal has been observed showing a maximum within the transistor channel and close to the source contact [12,13]. This maximum was attributed to the release of trapped holes after the interaction of triplet excitons created by the laser light with hole-trapping states. It was concluded that the SPCM technique is a powerful technique for monitoring the distribution of the trapped holes along the channel of pentacene FETs under different operating conditions, which determines the spatial variation of the upward band bending. However, the magnitude of the upward band bending along the accumulation layer was not determined.

An important parameter governing the SPCM signal is the frequency of the modulated laser light. Westermeier et al. [12] employing frequency-resolved SPCM (FR-SPCM), found a non-uniform decrease in the photocurrent along the transistor channel when the frequency of the modulated laser light was increased. The above authors attributed this frequency dependence to trapping and release events occurring on different time scales. In the present work, FR-SPCM measurements are employed to elucidate the microscopic processes governing the frequency dependence of photocurrents in pentacene FETs. For the analysis and interpretation of these measurements, the frequency dependence of the photocurrents of organic two-terminal devices studied previously is considered very useful to interpret the present results [14,15]. To this end, a detailed comparison of the FR-SPCM with the photocurrent spectra of the two-terminal devices is made. It is examined whether the methods applied to photocurrent spectra can also be applied to the FR-SPCM of three-terminal devices. This way, it will be possible to extract information on critical parameters that determine the performance of FETs, such as the energy distribution of pentacene trap states at the insulator interface as well as the band bending along the accumulation layer induced by the gate voltage.

2. Experimental Details

Pentacene FETs were fabricated on substrates of heavily doped n-type c-Si, which served as a back-gate electrode by having a 500 nm thick thermally grown SiO₂ layer on the top surface. A 150 nm PMMA layer was spin-coated on the SiO₂ layer and annealed at 100 °C. The substrates were then placed in the deposition chamber, where a 240 nm polycrystalline pentacene layer was evaporated on the PMMA layer at a stabilized deposition rate of 2 nm min^{−1} under a base vacuum of 1.2×10^{-6} Torr. On the top surface of the pentacene layer, 50 nm thick gold was evaporated at a deposition rate of 0.14 nm/min to form the source and drain electrodes of 6 mm length and 450 μm separation through a shadow mask. The fabricated devices were placed in an optical cryostat in which all the measurements were performed at a temperature of about 19 °C and under a base vacuum of 3×10^{-3} Torr to minimize the effects of environmental impurities, which can affect the photocurrent [16].

The experimental setup of the SPCM technique has been presented elsewhere [13]. In this technique, light from a HeNe laser emitting at a 633 nm wavelength was passed through a mechanical chopper to produce an intensity-modulated light beam with a frequency ranging between 10-Hz and 10-kHz. The modulated light beam through a cylindrical lens was focused on the channel of the FET mounted on the optical cryostat. The focused laser beam was in the form of a thin 50 μm wide light bar oriented parallel to the two

gold surface electrodes and was used as a probe light beam scanned along the 450 μm conducting channel of the transistor. The relative position, x , of the probe laser beam measured from the source contact edge was determined by measuring the intensity of the laser light reflected from the surface. The laser light focused within the conducting channel of the transistor produces a varying source–drain current or a modulated photocurrent during the transistor operation with the selected drain-source V_{DS} and gate-source V_{GS} voltages. The I_{p} amplitude of this modulated photocurrent was amplified and measured with a digital lock-in amplifier (Stanford Research Systems SR830). The I_{p} measurements were performed for a given modulation frequency f of the chopper as a function of position x , providing the SPCM $I_{\text{p}}(x)$ profile, or for a given x as a function of angular frequency $\omega = 2\pi f$, providing the FR-SPCM $I_{\text{p}}(\omega)$ spectrum.

3. Results

3.1. SPCM Profiles

The spatial photocurrent $I_{\text{p}}(x)$ profiles, obtained by setting the chopper to the lowest frequency of $f = 10$ Hz and scanning the laser beam along the transistor channel at different positions, x , from the source edge, are shown in Figure 1 for constant $V_{\text{DS}} = -10$ V and different negative V_{GS} ranging from -5 V to -15 V. For less-negative V_{GS} values down to -6.5 V, the $I_{\text{p}}(x)$ signal in the channel is very low indicating that the transistor is in the off-state and the channel is depleted of charge carriers. By reducing the negative V_{GS} values to -8 V and -9.5 V, holes are accumulated at the pentacene insulator interface and the transistor switches to the on-state. During this transition, the $I_{\text{p}}(x)$ signal on the source side increases showing a maximum at a distance $x = 70$ μm from the source, whereas the $I_{\text{p}}(x)$ signal on the drain side remains at nearly zero. For V_{GS} lower than -9.5 V, the maximum of the $I_{\text{p}}(x)$ signal increases strongly, whereas the $I_{\text{p}}(x)$ signal on the drain side starts to increase.

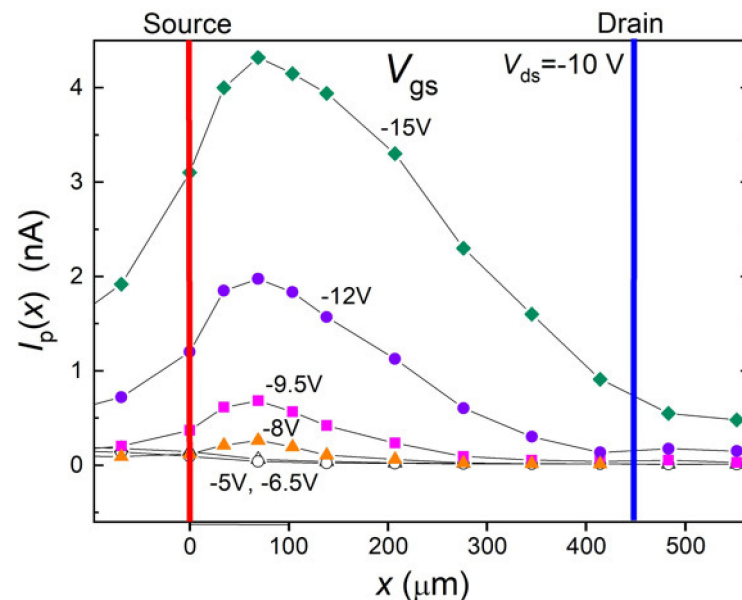


Figure 1. Spatial photocurrent $I_{\text{p}}(x)$ as a function of distance x measured from the source edge for the indicated voltages: -5 V (open circles), -6.5 V (open triangles), -8 V (orange triangles), -9.5 V (magenta squares), -12 V (blue circles), -15 V (olive diamonds). Increasing the negative V_{GS} above -6.5 V and keeping the V_{DS} constant, the transistor gradually transits from the off-state, where $I_{\text{p}}(x)$ is almost zero, to the on-state, in which the $I_{\text{p}}(x)$ signal starts to increase first near the source for $V_{\text{GS}} = -8$ V and -9.5 V and then at the drain side for more negative gate voltages ($V_{\text{GS}} < -9.5$ V).

The behavior of the SPCM profiles in Figure 1 can be rationalized by considering that local modulated laser excitation induces a modulated density $p_{ac}(x)$ per unit area of free holes (majority carriers) contributing to the signal $I_p(x)$ according to [6,13]

$$I_p(x) = \mu(x) p_{ac}(x) e W E(x) \quad (1)$$

where $\mu(x)$ is the local intrinsic hole mobility and $E(x)$ is the local lateral electric field along the channel. The modulated density $p_{ac}(x)$ of the holes is produced by the dissociation of the triplet excitons generated by the ultrafast singlet exciton fission process within the pentacene layer during each half-period of the chopped laser illumination [17]. However, the triplet excitons dissociation into mobile holes is a low probability process that can be assisted by a high electric field. Such a high electric field may occur near the edges of the contacts due to a large voltage drop caused by significant contact resistance producing a local maximum photocurrent at the contacts [9–11]. However, such a maximum in Figure 1 is not observed at the source or drain contact edges, indicating low contact resistance. Therefore, all the applied V_{DS} voltage drops take place along the conducting channel of the transistor, which has the highest resistance due to the long channel length. An additional electric field perpendicular to the insulator interface is generated by the applied gate V_{GS} voltage. However, this field should be high enough to facilitate the exciton dissociation and this can occur for most negative V_{GS} gate-source voltages [18].

Based on our previous analysis of the experimental results of SPCM in pentacene FETs [13], the dissociation of the triplet excitons is mainly realized by the so-called hole-detrapping mechanism [19]. According to this mechanism, triplet excitons diffusing in the pentacene layer can encounter trapped holes in the accumulation layer and interact with them. During this interaction, the electron of the triplet can recombine with the trapped hole. A hole is then released, increasing the density $p_{ac}(x)$ of detrapped holes contributing to the $I_p(x)$ signal according to Equation (1). In this way, the inhomogeneous spatial profiles $I_p(x)$ along the transistor channel of Figure 1 mainly reflect an inhomogeneous density of detrapped holes $p_{ac}(x)$. This density in turn comes from the inhomogeneous pattern of the trapped-hole density $N_t(x)$ along the pentacene–insulator interface due to inhomogeneous band bending.

As the transistor is turned on for $-9.5 \text{ V} < V_{GS} < -6.5 \text{ V}$, the $I_p(x)$ signal of Figure 1 starts to increase only on the source side. This indicates that the negative gate voltage exceeds a threshold limit and the local negative gate potential Ψ_S starts to increase creating upward band bending $-e\Psi_S$, shown schematically with the red upward arrows in Figure 2. As the valence band of pentacene bends upward, deeper donor-like trap states (blue solid circles), which were initially in a neutral state and empty of holes below the E_{tp} level, are lifted above the E_{tp} level and become positively charged filled by trapped holes (red circles). These holes can be detrapped from the triplets when the laser beam probes the source side, producing the onset of an increase in the $I_p(x)$ signal (Figure 1). In contrast, near the drain the $I_p(x)$ signal remains low, suggesting that there is no upward band bending because the negative gate voltage is canceled by the negative drain voltage $V_{DS} = -10 \text{ V}$. By decreasing the V_{GS} beyond -9.5 V , the $I_p(x)$ signal starts to increase on the drain side as well. This indicates that the negative effective gate voltage is not completely canceled out by the negative drain voltage and can now produce negative gate potential and upward band bending on the drain side as well. When the transistor is in the on-state, the $I_p(x)$ profile shows a gradual decrease towards the drain, as in Figures 1 and 3 with $V_{GS} = -12$, -15 , and -20 V . This reflects a decrease in $N_t(x)$ density and upward band bending due to the moderate and applied negative $V_{DS} = -10 \text{ V}$, which provides that the transistor is operating in the saturation region for the above V_{GS} voltages, as confirmed from the output characteristics (not shown).

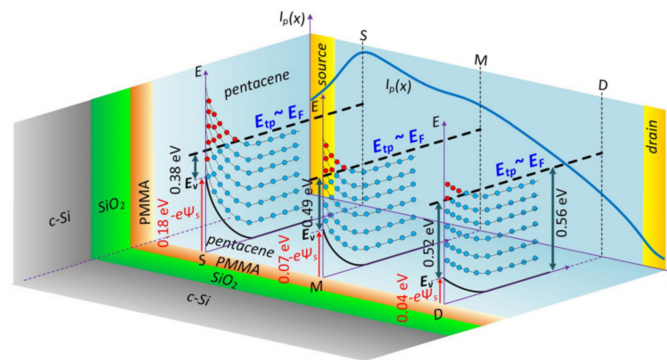


Figure 2. Schematic representation of the upward band bending at pentacene insulator interface for different positions in the transistor channel. The magnitude of the band bending $-e\Psi_s$ (red arrows) from the negative V_{GS} voltage is deduced from the listed energy gaps ($E_{tp} - E_v$) obtained from the SR-SPCM spectra by placing the laser beam near the source (S), midway between the source and drain (M), and near the drain (D). Note that only the relative positions of E_{tp} and E_v levels can be determined. Their variation along the channel due to the applied $V_{DS} = -10$ V cannot be deduced from our measurements. However, this voltage produces a reduction in $-e\Psi_s$ from source to drain, which is captured by the increase in the energy gap ($E_{tp} - E_v$). Due to the band bending, empty hole traps (blue circles) are lifted above the E_{tp} level and become filled with trapped holes (red circles) in the accumulation layer at the insulator interface, The $I_p(x)$ profile (solid blue line) obtained for $V_{GS} = -20$ V and $V_{DS} = -10$ V reflects the inhomogeneous profile of trapped holes (red solid circles).

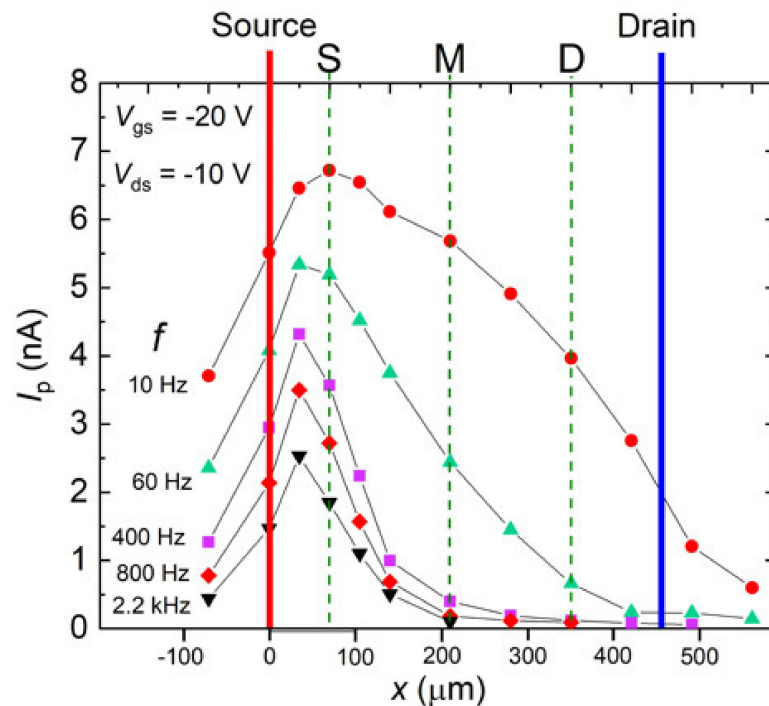


Figure 3. Photocurrent $I_p(x)$ as a function of distance x from the source edge for the indicated chopper frequencies f : 10 Hz (red circles), 60 Hz (green up triangles), 400 Hz (magenta squares), 800 Hz (red diamonds), 2.2 kHz (black down triangles). An overall reduction in $I_p(x)$ that is relatively stronger on the drain side is produced by increasing f .

3.2. FR-SPCM Spectra

Figure 3 presents the $I_p(x)$ profile of the photocurrent along the transistor channel obtained for different chopper frequencies f ranging from 10 Hz to 2.2 kHz. The applied voltages were $V_{GS} = -20$ V and $V_{DS} = -10$ V, which set the transistor in the saturation region. It is obvious that the increase in the chopper frequency f causes an overall reduction

in the photocurrent $I_p(x)$ in the whole channel. However, this reduction is relatively stronger on the drain side so that at the highest frequencies only the photocurrent near the source can be measured.

Westermeier et al. [12] reported FR-SPCM measurements and found a decrease in the photocurrent with increasing frequency, which is similar to that found here in the $I_p(x)$ profiles in Figure 3. This dependence was attributed to trap-and-release events occurring at different time scales ranging from milliseconds to microseconds without specifying the energy level of the associated traps and their distribution [12].

Here FR-SCPM measurements are employed to explore the microscopic processes responsible for the decrease in the photocurrent with frequency. For this purpose, the photocurrent was measured as a function of the angular modulation frequency $\omega = 2\pi f$ by placing the probe laser beam at three different positions within the channel shown by the dashed vertical lines in Figure 3. These lines, denoted as (S), (M), and (D), correspond to laser illumination near the source, midway between the source and drain, and near the drain, respectively. The $I_p(\omega)$ spectra of the different locations in the channel cannot be directly compared because the magnitude of $I_p(x)$ is varied along the channel by the variations in the band bending. However, we found that if the $I_p(\omega)$ spectra are shifted vertically, they match each other at higher frequencies, as shown in Figure 4a. In particular, the resulting $I_p(\omega)$ spectra of Figure 4a after the appropriate vertical shifts, are merged at higher frequencies, defining the $I_{po}(\omega)$ spectrum that has the form of an upper envelope (solid line) from all $I_p(\omega)$ spectra. The $I_{po}(\omega)$ values of this envelope show a relatively strong decrease with increasing frequency, which is almost independent of the x position of the probe illumination in the channel. Moreover, each $I_p(\omega)$ spectrum shows at a frequency ω_s (vertical dashed lines) a crossover from the strong frequency dependence at a higher ω to a much weaker frequency dependence at a lower ω . The crossover frequency ω_s is observed at a high, intermediate, and low frequency for the spectra with probe laser illumination on the source side (S), midway through the channel (M), and on the drain side (D), respectively. The above behavior of the $I_p(\omega)$ spectra resembles the corresponding behavior observed earlier in the photocurrent spectra of organic two-terminal devices [15,20], which are presented below for a detailed comparison with the present spectra.

3.3. Detailed Comparison with the Photocurrent Spectra of Two-Terminal Devices

The effect of light modulation frequency on the photocurrent has been previously studied in organic two-terminal devices on a glass substrate [15,20]. In these devices, the entire area of the organic semiconductor in the conducting channel, including the area of two parallel surface gold contacts, is uniformly illuminated by two beams of light from red light-emitted diodes with a maximum emission of 630 nm. One beam is called a probe light beam and its intensity is modulated by producing a modulated photocurrent (MPC) with amplitude I_{ac} , which is measured by a lock-in amplifier as a function of the angular modulation frequency ω . The second light beam provides a constant-intensity continuous-wave (*cw*) bias illumination called a bias beam. A typical example of the MPC $I_{ac}(\omega)$ spectra of two-terminal pentacene devices obtained with different intensities of the *cw* bias light beam is shown in panel (d) of Figure 4 and similar $I_{ac}(\omega)$ spectra were observed in rubrene crystals. From the analysis of these spectra, it was concluded that the hole transport (majority carriers) in rubrene [20] and pentacene [15] occurs according to the multiple trapping and release (MTR) model. In this model, the transport of the photogenerated mobile holes takes place at the valence band edge E_V . Hole transport is interrupted by trapping and thermal release from traps.

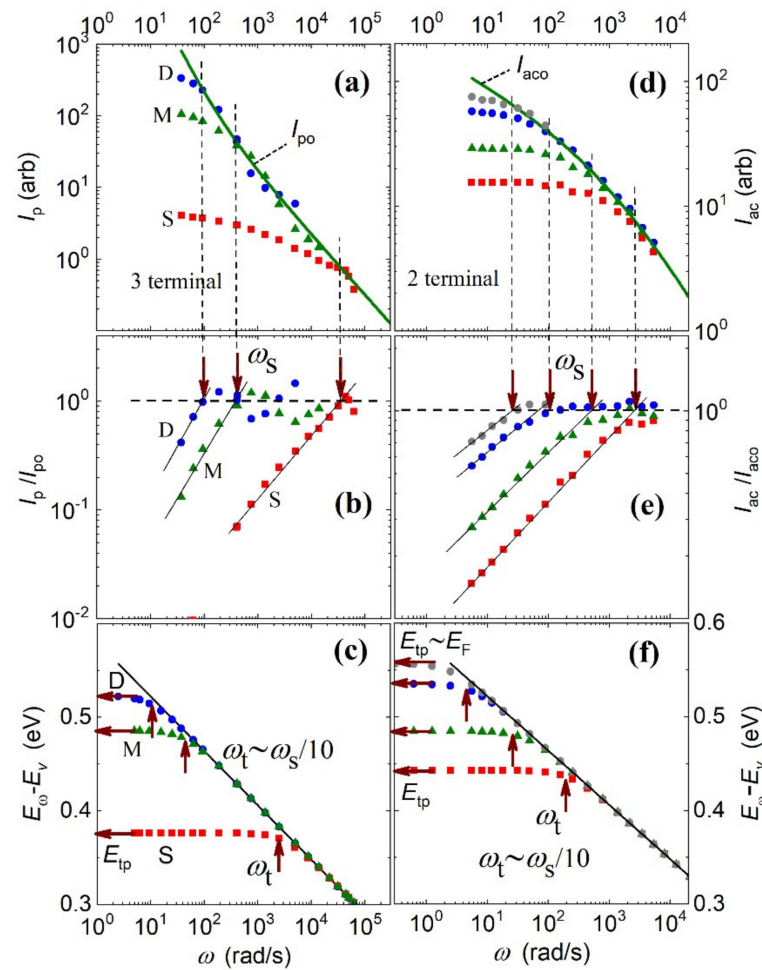


Figure 4. Photocurrent spectra of three-terminal pentacene FETs compared with the photocurrent spectra of two-terminal pentacene films on glass substrate. Spectra of photocurrent $I_p(\omega)$ (a), $I_p(\omega)/I_{po}(\omega)$ ratio (b), and probed trap depth ($E_\omega - E_v$) (c) of pentacene FETs obtained for probe laser beam placed near the source (S) (red squares), midway the source and drain (M) (olive triangles), and near the drain side (D) (blue circles). Spectra of the MPC amplitude $I_{ac}(\omega)$ (d), $I_{ac}(\omega)/I_{aco}(\omega)$ ratio (e), and probed trap depth ($E_\omega - E_v$) (f) of pentacene two-terminal devices typically obtained by increasing intensity of the bias light: 1.2×10^{11} (grey circles), 7.5×10^{11} (blue circles), 4×10^{12} (olive triangles), 1.8×10^{13} (red squares) photons $\text{cm}^{-2} \text{s}^{-1}$. Down and up arrows indicate frequencies ω_s and ω_t , respectively. Horizontal arrows indicate E_{tp} level. Solid straight lines indicate ($E_\omega - E_v$) calculated from Equation (5).

The role of the light probe beam modulated at frequency ω in the two-terminal devices is to selectively probe only specific active traps that have density $N(E_\omega - E_v)$ within an energy interval kT around the probe energy E_ω that contributes to the MPC amplitude $I_{ac}(\omega)$. The holes created by the probe light interact through trapping and thermal release with the probed active traps at the trap depth ($E_\omega - E_v$) level with a thermal emission rate that satisfies the following condition [21]

$$e_p(E_\omega - E_v) = \nu_o \exp\left(-\frac{E_\omega - E_v}{kT}\right) = \sqrt{\omega^2 + \omega_t^2} \quad (2)$$

where ν_o is the attempt to escape frequency found to be of the order of 10^{10} s^{-1} in pentacene films [14]. ω_t is the characteristic trapping frequency given by $\omega_t = pc_p + nc_n$, with p and n representing the steady-state mobile holes and electron concentrations and c_p and c_n representing the carrier capture coefficients of the traps for holes and electrons, respectively. Assuming that the photocurrent is due to mobile holes, with virtually all electrons trapped,

we have $\omega_t \cong pc_p$, reflecting the fact that ω_t is controlled by the intensity of bias illumination. The probed trap-depth energy ($E_\omega - E_v$) is thus given by [21]

$$E_\omega - E_v = kT \ln \left(\frac{v_o}{\sqrt{\omega^2 + \omega_t^2}} \right) \quad (3)$$

The energy E_{tp} of the quasi-Fermi level corresponding to the upmost filled hole trap states and measured from the valence band edge E_v is given by

$$E_{tp} - E_v = kT \ln(v_o/\omega_t) \quad (4)$$

Therefore, for a given intensity of the cw bias beam and a given modulation frequency ω of the probe beam, the active trap states at trap depth ($E_\omega - E_v$) given by Equation (3) would provide the maximum contribution to the MPC $I_{ac}(\omega)$ through the trapping/detrapping processes.

The high probe's modulation frequency ($\omega \gg \omega_t$), ω_t in Equations (2) and (3) can be neglected, and the thermal emission rate from the probed states at E_ω becomes equal to the modulation frequency of the probe beam, $e_p(E_{\omega_o} - E_v) \cong \omega$. In this case, the probe energy level reduces to $E_\omega \cong E_{\omega_o}$ and is given by

$$E_{\omega_o} - E_v \cong kT \ln \left(\frac{v_o}{\omega} \right) \quad (5)$$

Equation (5) shows that by scanning the modulation frequency ω at frequencies much higher than the respective ω_t ($\omega \gg \omega_t$), the probed energy level E_{ω_o} shifts to different trap energy levels shown by the solid straight line in Figure 4f. These correspond to empty hole trap states that are shallower than the respective E_{tp} levels (horizontal arrows). Correspondingly, the probed energy level E_{ω_o} , as well as the amplitude $I_{aco}(\omega)$, are almost independent of ω_t and therefore insensitive to the intensity of the bias beam. This situation obtained for $\omega \gg \omega_t$ corresponds to the so-called high frequency (HF) regime corresponding to the upper envelope (solid line) of all $I_{ac}(\omega)$ spectra in Figure 4d. This envelope consists of a range of values $I_{ac}(\omega) = I_{aco}(\omega)$ that are almost independent of the intensity of the bias beam and the respective ω_t . As mentioned above, very similar behavior is observed in the $I_p(\omega)$ spectra of three-terminal devices (Figure 4a), which also merge at higher ω forming a similar upper envelope of $I_{po}(\omega)$ values. Therefore, in the $I_p(\omega)$ spectra there is also an analogous HF regime, which includes values of the upper envelope $I_p(\omega) = I_{po}(\omega)$ that are independent of the respective characteristic trapping frequency ω_t . This indicates that, similar to the MPC $I_{aco}(\omega)$ signal, the main contribution to the SPCM $I_{po}(\omega)$ signal comes from active probed trap states at trap depth ($E_{\omega_o} - E_v$) that have density $N(E_{\omega_o} - E_v)$ with which the holes interact via trapping/detrapping. The expression relating the $I_{aco}(\omega)$ signal to the probed trap density $N(E_{\omega_o} - E_v)$ presented earlier in Equation (50) of Ref. [21] can be written in the following simple form

$$I_{aco}(\omega) = C/N(E_{\omega_o} - E_v), \quad (6)$$

where C is a constant containing several parameters essentially independent of the frequency ω . Therefore, the distribution of the probed traps can be obtained from the following relations

$$N(E_{\omega_o} - E_v) \propto (I_{aco}(\omega))^{-1} \text{ and } N(E_{\omega_o} - E_v) \propto (I_{po}(\omega))^{-1} \quad (7)$$

for the two- and three-terminal devices, respectively.

The tap distributions, as calculated according to Equation (7), are plotted in Figure 5 as a function of the probed trap depth ($E_{\omega_o} - E_v$) calculated from Equation (5). The $N(E_{\omega_o} - E_v)$ distributions show a nearly exponential dependence with the indicative characteristic E_o energies 35 meV and 30 meV at the shallower trap depths for the two-

and three-terminal devices, respectively. At deeper trap depths, the trap distribution (blue solid line) of the FETs is found to be steeper than that of the two-terminal devices (red dashed-dotted line). It should be noted that the $N(E_{\omega_0} - E_V)$ distribution of the FETs refers to the trap distribution of the first few pentacene monolayers at the insulator interface that make the dominant contribution to the $I_{po}(\omega)$ signal.

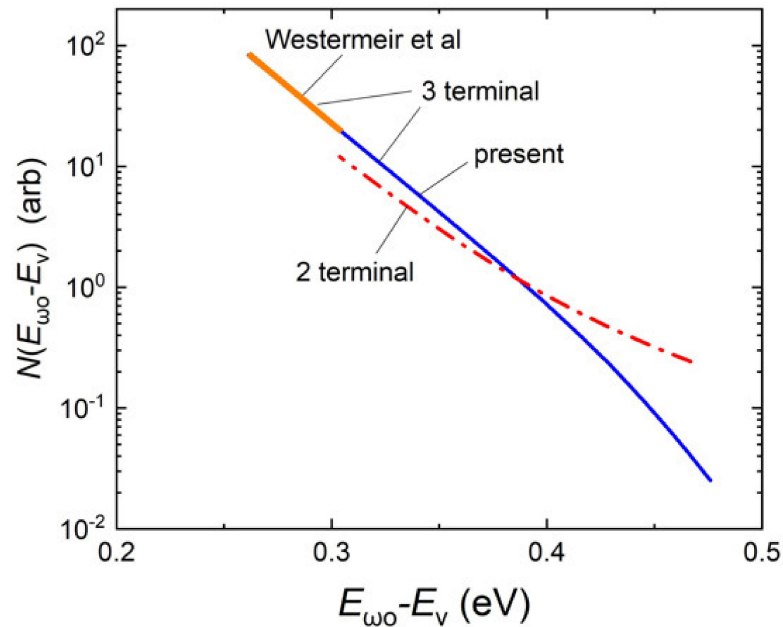


Figure 5. The active probed trap distributions $N(E_{\omega_0} - E_V)$ of the two- and three-terminal pentacene devices as a function of the probed trap depth ($E_{\omega_0} - E_V$). The trap distributions were calculated from Equation (7) using the $I_{aco}(\omega)$ values of Figure 4d and the $I_{po}(\omega)$ values of our transistor from Figure 4a and the $I_{po}(\omega)$ values of the transistor of Westermeir et al. [12] presented below in Figure 7.

The role of the cw bias illumination, on the other hand, in two-terminal devices is to excite an excess density of mobile holes in the valence band. These holes would quickly relax into the tail of localized states filling the exponential trap tail states, starting from the deepest levels (deep traps) and up to the characteristic energy level of the quasi-Fermi level of trapped holes E_{tp} . The more photocarriers produced, the more trap states in the tail are filled, and thus the closer the E_{tp} level gets to the transport path at the valence band edge at E_V . This shift in the E_{tp} level is directly reflected in the MPC $I_{ac}(\omega)$ spectra in Figure 4d with the apparent shift to higher frequencies of the crossover frequency ω_s (vertical dashed lines). At ω_s , a crossover is observed where the $I_{ac}(\omega)$ signal exhibits a transition from a strong to a much weaker frequency dependence before reaching a plateau or saturation at a lower ω . This plateau signifies the so-called low frequency (LF) regime that occurs for $\omega \ll \omega_t$. The crossover frequencies ω_s are determined from the spectra of the $I_{ac}(\omega)/I_{aco}(\omega)$ ratio from Figure 4e calculated by dividing the $I_{ac}(\omega)$ spectra by the $I_{aco}(\omega)$ spectrum from Figure 4d. It can be seen that each ratio $I_{ac}(\omega)/I_{aco}(\omega)$ in Figure 4e is close to unity (horizontal solid line) at higher frequencies ($\omega \gg \omega_t$) that define the HF regime. Around each ω_s and lower frequencies, the $I_{ac}(\omega)/I_{aco}(\omega)$ ratio drops sharply following approximately a straight line. The extrapolation of this line intersects the horizontal solid line at the crossover frequency ω_s (down arrow), defining the crossover from the HF to the LF regime. The crossover frequency ω_s is used to determine the characteristic trapping frequency ω_t , considering that ω_t is approximately [20]

$$\omega_t \approx \omega_s/10 \quad (8)$$

The ω_t , from Equation (8) is introduced in the more general Equation (3) to determine the probe energy level E_ω , depicted in panel (f) in Figure 4 (symbols), of the corresponding $I_{ac}(\omega)$ spectra. By decreasing ω below ω_s , the probed energy level E_ω in Figure 4f shifts

progressively slowly toward the corresponding quasi-Fermi level E_{tp} , (horizontal arrows). Finally, in the LF regime where the $I_{ac}(\omega)$ has reached a plateau, E_{ω} is very close to E_{tp} and hardly shifts by changing ω , confirming that the LF regime has indeed been reached and that Equation (8) is a good approximation. Moreover, Equation (8) can be introduced into Equation (4) to obtain

$$E_{tp} - E_v = kT \ln(10 \nu_o / \omega_s) \quad (9)$$

which is very useful as it provides an estimate of the energy gap ($E_{tp} - E_v$). Taking advantage of this, we can determine the energy gap ($E_F - E_v$). Particularly, in the case of the spectrum in Figure 4d obtained with the lowest intensity of the bias light (open circles), the current under illumination is comparable to the dark current. Therefore, the corresponding quasi-Fermi E_{tp} level (horizontal dashed line) estimated at 0.56 eV above E_v is very close to the Fermi level E_F and can be considered an estimation of the E_F level: ($E_{tp} - E_v$) \approx ($E_F - E_v$) \approx 0.56 eV.

It should be emphasized that the characteristic variations in the $I_p(\omega)$ spectra in Figure 4a obtained by focusing the laser light beam at various positions along the transistor channel, are qualitatively very similar to the variations in the $I_{ac}(\omega)$ spectra in Figure 4d obtained by varying the intensity of the bias light. A crossover from the HF to the LF regime also occurs in the $I_p(\omega)$ spectra of three-terminal devices at the crossover frequency ω_s (vertical dashed lines). This frequency is determined from the ratio $I_p(\omega)/I_{po}(\omega)$ (Figure 4b), as in the case of the two-terminal devices (Figure 4e) described above. The corresponding characteristic trapping frequency ω_t can be then estimated from the frequency ω_s using Equation (8). Since the ω_s in Figure 4a,b shifts to a higher frequency as the probe laser beam is placed progressively closer to the source, accordingly, the ω_t calculated from Equation (8) shifts progressively to a higher ω .

3.4. Estimation of the Band Bending from the $I_p(\omega)$ Spectra

The shift of the ω_t to higher frequencies in the $I_p(\omega)$ spectra observed above when the probe laser beam is displaced from the drain to the source side shows that the corresponding energy gap ($E_{tp} - E_v$) calculated from Equation (9) is gradually decreasing. However, the E_{tp} level during the SPCM measurements remains fixed in its equilibrium state near the E_F level as shown in Figure 2 (dashed black line). This is because the photocurrent remains usually comparable to or lower than the source–drain dark current. Considering the zero of the energy scale at the E_{tp} level, which as mentioned above is essentially at the E_F level, the calculated ($E_{tp} - E_v$) shown in Figure 6 (solid blue circles) represents the relative position of the edge E_v below the E_{tp} or E_F level along the channel of the transistor. In this calculation, we used in Equation (9) either the attempt-to-escape frequency $\nu_o = 10^{10} \text{ s}^{-1}$ (left axis) previously obtained from our two-terminal pentacene devices [14] or the lower limit $\nu_o = 10^8 \text{ s}^{-1}$ (right axis) recently obtained from rubrene crystals [20]. In Figure 6, the valence band E_v edge is closer to the E_{tp} level on the source side, manifesting the increase of the upward band bending $-e\Psi_s$, shown graphically in Figure 2. Toward the drain, the E_v moves away from the E_{tp} or E_F level due to the applied $V_{ds} = -10 \text{ V}$ causing a gradual decrease in the upward band bending.

As is evident in Figure 2, the corresponding upward band bending $-e\Psi_s$ (red arrows) can be calculated from $-e\Psi_s \approx (E_F - E_v) - (E_{tp} - E_v)$. The energy gap ($E_{tp} - E_v$) was obtained above from the $I_p(\omega)$ using Equation (9). The energy gap ($E_F - E_v$) \approx 0.56 eV from the E_F level to the valence band E_v edge without upward band bending was obtained from the $I_{ac}(\omega)$ spectra in the previous section. The calculated $-e\Psi_s$ listed in the graph in Figure 2 increases gradually from 0.04 eV near the drain to 0.07 eV midway through the channel, and finally to 0.18 eV near the source.

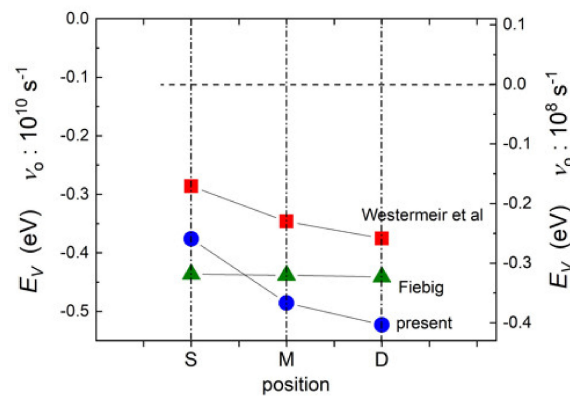


Figure 6. Valence band edge energy E_V below the E_{tp} level along the channel of FETs from different laboratories. The energy E_V was calculated from Equation (9) using the crossover frequencies ω_s of the corresponding $I_p(\omega)$ spectra in Figure 6 of our transistor (circles) and the transistors of Westermeir et al. [12] (squares) and Fiebig [22] (triangles), for $\nu_o = 10^{10} \text{ s}^{-1}$ (left axis) and $\nu_o = 10^8 \text{ s}^{-1}$ (right axis).

3.5. Application of Our Analysis to the FR-SPCM Data of Other Authors

Photocurrent profiles $I_p(x)$ along the channel of the FETs for different modulation frequencies ω of the probe laser beam have been reported by Westermeir et al. [12] and Fiebig [22]. We digitized these results from which we extracted the frequency dependence of the photocurrent, i.e., the $I_p(\omega)$ spectra near the source (S), in the middle between the source and drain (M), and near the drain (D), as in our device. For comparison, these spectra were vertically shifted to match at higher ω with each other and with the $I_p(\omega)$ spectra in Figure 4a. The resulting $I_p(\omega)$ spectra of all devices are plotted in Figure 7. From this figure, it is remarkable that the frequency dependence of the photocurrent $I_p(\omega)$ of all the different devices is very similar. In particular, by extrapolating at higher ω , the upper envelope $I_{po}(\omega)$ (solid green line) of our $I_p(\omega)$ spectra, we obtain the upper envelope $I_{po}(\omega)$ (solid orange line) corresponding to the HF regime of the $I_p(\omega)$ spectra (open squares) of Westermeir et al. [12]. These authors have performed SPCM measurements up to over ten times' higher frequencies. The $N(E_{\omega_0} - E_V)$ trap distribution derived from the $I_{po}(\omega)$ spectra of Westermeir et al. [12] via Equation (7) is also exponential with $E_o = 30 \text{ meV}$ shown in Figure 5 (orange solid line) and is the extension at shallower trap depths of the exponential $N(E_{\omega_0} - E_V)$ distribution derived from our device.

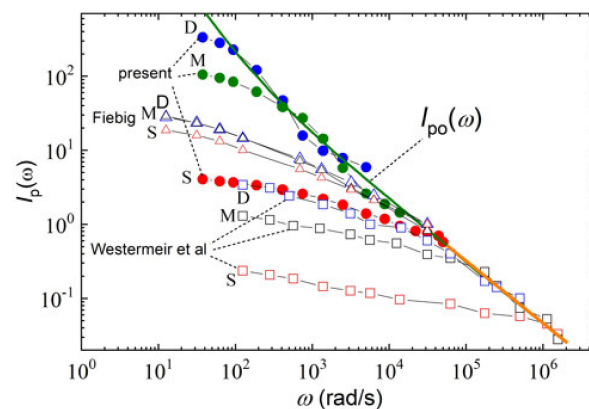


Figure 7. Photocurrent $I_p(\omega)$ spectra as a function of the angular modulation frequency of FETs from different laboratories. The $I_p(\omega)$ signal is shown for probe laser illumination near the source (S), midway between the source and drain (M), and near the drain side (D). $I_p(\omega)$ signal derived by digitizing the SPCM $I_p(x)$ profiles of different modulation frequencies reported by Westermeir et al. [12] (open squares) and Fiebig [22] (open triangles). The $I_p(\omega)$ spectra of the present work (solid circles) are taken from Figure 4a.

In the $I_p(\omega)$ spectra in Figure 7, the characteristic transition from the HF to the LF regime is observed in all devices. By decreasing the frequency below the respective crossover at ω_s , the $I_p(\omega)$ signal shows a very similar weak frequency dependence without, however, the characteristic saturation in the LF regime observed in the $i_{ac}(\omega)$ spectra of two-terminal devices (Figure 4f). This can be attributed to the fact that the upward band bending in the pentacene accumulation layer vanishes within the Debye length L_D , which includes about 2–3 pentacene monolayers above the insulator interface. In the first monolayer, the upward band bending is the highest and thus this layer has the highest density of trapped holes and the highest effective contribution to the $I_p(\omega)$ signal. Therefore, the characteristic transition from the HF to the LF regime and the saturation of the photocurrent produced from the first monolayer are expected at relatively higher frequencies. The respective lower contribution to $I_p(\omega)$ from the subsequent monolayers with the lower band bending is expected to continue to increase with decreasing ω and to saturate at lower frequencies. This may provide an increasing small contribution to the $I_p(\omega)$ signal at lower ω that can explain the weak increase in the $I_p(\omega)$ signal in the LF regime.

Using Equation (9), we calculated the position of E_v with respect to E_{tp} using the corresponding crossover frequencies ω_s , as determined from the $I_p(\omega)$ spectra in Figure 7, and the results from all the devices are presented in Figure 6. Similar to our device, the device of Westermeier et al. [12] also operates in the saturation region by applying the same voltages $V_{GS} = -20$ V and $V_{DS} = -10$ V, and the E_v edge from the drain to the source is also getting closer to the E_{tp} or E_F level. Therefore, an inhomogeneous upward band bending is confirmed along the channel, which is typical for transistors operating in the saturation region. In contrast, in Fiebig's device [22], operating in the linear region with $V_{GS} = -30$ V and $V_{DS} = -5$ V, the edge E_v is at about the same energy below the E_{tp} or E_F level throughout the transistor channel (Figure 6). This indicates that the valence band bends up uniformly along the channel providing a constant upward band bending, which is characteristic of FETs operating in the linear region. This uniform band bending is further supported by the nearly uniform photocurrent profile $I_p(x)$ reported by Fiebig for this transistor operating in the linear region [22].

Finally, it is important to note that in all the examined FETs presented in Figure 6, the edge E_v is located below the E_F level assuming either attempt-to-escape frequency $\nu_o = 10^{10} \text{ s}^{-1}$ or the relatively lower $\nu_o = 10^8 \text{ s}^{-1}$. Therefore, the upward band bending for the applied $V_{GS} = -20$ V or -30 V is not sufficient for the E_F level to enter the valence band.

4. Conclusions

The presented experiments confirm that the SPCM $I_p(x)$ profile can be used to monitor variations in the upward band bending along the conducting channel of pentacene FETs during turn-on and during their operation with different applied voltages. The FR-SPCM $I_p(\omega)$ spectra obtained by placing the laser probe beam at different positions within the channel between the source and drain were found to be very similar to the MPC spectra of the two-terminal pentacene devices obtained by changing the intensity of the bias light. As is the case with the photocurrent $I_{ac}(\omega)$ spectra of two-terminal devices, the $I_p(\omega)$ spectra of FETs are associated with trap and release events in active empty probed trap states. These traps, which contribute effectively to the $I_p(\omega)$ signal, are selected by the modulation frequency of the probe laser beam. This allows us to use the FR-SPCM as a spectroscopic technique to determine the energy distribution of the active trap states of the first pentacene monolayers along the pentacene insulator interface, which are critical in controlling the performance of OFETs. Furthermore, the method applied to the MPC $I_{ac}(\omega)$ spectra to estimate the energy gap of the quasi-Fermi E_{tp} level from the valence band edge E_v can also be applied to the $I_p(\omega)$ spectra. In this way, the shift of the valence band edge E_v towards the E_{tp} or E_F level from the upward band bending caused by the negative gate voltage can be monitored along the conducting channel of organic FETs. The applicability of our methods was confirmed in the FR-SPCM data of pentacene FETs reported by other authors.

Author Contributions: Data curation, G.K. and N.V.; writing—original draft, A.G.; idea, writing—review & editing, P.K. All authors have read and agreed to the published version of the manuscript.

Funding: This research received no external funding.

Conflicts of Interest: The authors declare no conflict of interest.

References

1. Ostroverkhova, O. Organic Optoelectronic Materials: Mechanisms and Applications. *Chem. Rev.* **2016**, *116*, 13279. [[CrossRef](#)] [[PubMed](#)]
2. Yan, Y.; Zhao, Y.; Liu, Y. Recent progress in organic field-effect transistor-based integrated circuits. *J. Polym. Sci.* **2022**, *60*, 311. [[CrossRef](#)]
3. Wang, C.; Zhang, X.; Dong, H.; Chen, X.; Hu, W. Challenges and Emerging Opportunities in High-Mobility and Low-Energy-Consumption Organic Field-Effect Transistors. *Adv. Energy Mater.* **2020**, *10*, 2000955. [[CrossRef](#)]
4. Kim, C.H.; Bonnassieux, Y.; Horowitz, G. Charge distribution and contact resistance model for coplanar organic field-effect transistors. *IEEE Trans. Electron. Devices* **2013**, *60*, 280. [[CrossRef](#)]
5. Chua, L.L.; Zaumseil, J.; Chang, J.F.; Ou, E.C.W.; Ho, P.K.H.; Sirringhaus, H.; Friend, R.H. General observation of n-type field-effect behaviour in organic semiconductors. *Nature* **2005**, *434*, 194. [[CrossRef](#)]
6. Liewald, C.; Reiser, D.; Westermeier, C.; Nickel, B. Photocurrent microscopy of contact resistance and charge carrier traps in organic field-effect transistors. *Appl. Phys. Lett.* **2016**, *109*, 53301. [[CrossRef](#)]
7. Mathijssen, S.G.J.; Spijkman, M.J.; Andringa, A.M.; van Hal, P.A.; McCulloch, I.; Kemerink, M.; Janssen, R.A.J.; de Leeuw, D.M. Revealing buried interfaces to understand the origins of threshold voltage shifts in organic field-effect transistors. *Adv. Mater.* **2010**, *22*, 5105. [[CrossRef](#)] [[PubMed](#)]
8. Graham, R.; Yu, D. Scanning photocurrent microscopy in semiconductor nanostructures. *Phys. Lett. B* **2013**, *27*, 1330018. [[CrossRef](#)]
9. Jia, Z.; Banu, L.; Kyymissis, I. Photocurrent Study of Oxygen-Mediated Doping States in Pentacene Thin-Film Transistors. *IEEE Trans. Electron. Devices* **2010**, *57*, 380. [[CrossRef](#)]
10. Fiebig, M.; Erlen, C.; Göllner, M.; Lugli, P.; Nickel, B. Spatially resolved photoresponse measurements on pentacene thin-film transistors. *Appl. Phys. A* **2009**, *95*, 113. [[CrossRef](#)]
11. Tsen, A.W.; Cicoira, F.; Malliaras, G.G.; Park, J. Photoelectrical imaging and characterization of point contacts in pentacene thin-film transistors. *Appl. Phys. Lett.* **2010**, *97*, 23308. [[CrossRef](#)]
12. Westermeier, C.; Fiebig, M.; Nickel, B. Mapping of Trap Densities and Hotspots in Pentacene Thin-Film Transistors by Frequency-Resolved Scanning Photoresponse Microscopy. *Adv. Mater.* **2013**, *25*, 5719. [[CrossRef](#)]
13. Giannopoulou, A.; Kounavis, P. Visualization of channel formation of organic field-effect transistors by scanning photocurrent microscopy. *Org. Electron.* **2018**, *58*, 167. [[CrossRef](#)]
14. Gorgolis, S.; Giannopoulou, A.; Kounavis, P. Charge carriers' trapping states in pentacene films studied by modulated photocurrent. *J. Appl. Phys.* **2013**, *113*, 123102. [[CrossRef](#)]
15. Vagenas, N.; Giannopoulou, A.; Kounavis, P. Density and Mobility Effects of the Majority Carriers in Organic Semiconductors under Light Excitation. *J. Appl. Phys.* **2015**, *117*, 33105. [[CrossRef](#)]
16. Fraboni, B.; Matteucci, A.; Cavallini, A. Photocurrent studies of stress and aging in pentacene thin film transistors. *Appl. Phys. Lett.* **2006**, *89*, 222112. [[CrossRef](#)]
17. Smith, M.B.; Michl, J. Singlet Fission. *J. Chem. Rev.* **2010**, *110*, 6891. [[CrossRef](#)]
18. Lloyd-Hughes, J.; Richards, T.; Sirringhaus, H.; Johnston, M.B.; Herz, L.M. Exciton dissociation in polymer field-effect transistors studied using terahertz spectroscopy. *Phys. Rev. B* **2008**, *77*, 125203. [[CrossRef](#)]
19. Qiao, X.; Zhao, C.; Chen, B.; Luan, L. Trap-induced photoconductivity in singlet fission pentacene diodes. *Appl. Phys. Lett.* **2014**, *105*, 33303. [[CrossRef](#)]
20. Vagenas, N.; Podzorov, V.; Kounavis, P. Modulated-Photocurrent Spectroscopy of Single-Crystal Organic Semiconductor Rubrene with Pristine and Trap-Dominated Surfaces. *Phys. Rev. Mater.* **2021**, *5*, 63801. [[CrossRef](#)]
21. Kounavis, P. Analysis of the modulated photocurrent experiment. *Phys. Rev. B* **2001**, *64*, 45204. [[CrossRef](#)]
22. Fiebig, M. Spatially Resolved Electronic and Optoelectronic Measurements of Pentacene Thin Film Transistors. Ph.D. Thesis, Ludwig-Maximilians-Universität München, München, Germany, 2010.